



Full length article

Interaction of C, N and O interstitial solute atoms with screw dislocations in HfNbTaTiZr high entropy alloy

Thomas Leveau, Lisa Ventelon, Emmanuel Clouet ^{*,1}

Université Paris-Saclay, CEA, Service de recherche en Corrosion et Comportement des Matériaux, SRMP, 91191 Gif Sur Yvette, France

ARTICLE INFO

Keywords:

Dislocations

Plasticity

Ab initio

Body-centered cubic transition metals

High entropy alloy

ABSTRACT

Using density functional theory (DFT), we characterize the interaction of screw dislocations with interstitial impurities, in particular oxygen, nitrogen and carbon, in the HfNbTaTiZr alloy of body-centered cubic (BCC) structure. Considering different configurations representative of the disordered solid solution alloy, we evidence a noticeable core spreading of the screw dislocation whether with or without solute, associated with a wide range in dislocation-solute interaction energy, which is found to be mainly attractive for the three investigated impurities. This interaction energy is shown to be highly influenced by the type of the metal atoms in the neighbourhood of the solute. Notably the more BCC elements are present around the solute (either Nb or Ta), the more repulsive this interaction is.

1. Introduction

Over the past twenty years, a new class of alloys known as high entropy alloys (HEA) has emerged, in the search for new materials capable of competing with conventional alloys. Composed of multiple elements (usually five) close to equiatomic proportions, these alloys have been firstly designed with a face-centered cubic (FCC) structure [1,2] before being declined for high temperature applications in body-centered cubic (BCC) structure through the inclusion of refractory metals, known as refractory high entropy alloys (RHEA) [3–5]. Their high-temperature strength up to 0.6 of their melting temperature makes these alloys very promising for a wide range of structural high-temperature applications [6,7]. Several RHEA have been explored these last years and the attention here is focused on the HfNbTaTiZr RHEA. Developed for the first time by Senkov in 2011 [4], this concentrated BCC solid solution is ductile at room temperature, which makes it one material of choice for the experimental study of mechanical properties and hence a model RHEA.

Post-mortem observations by transmission electron microscopy on samples of HfNbTaTiZr have shown that the observed plastic deformation mechanisms are similar to those in dilute BCC alloys: plasticity is governed at room temperature by the motion of screw dislocations of Burgers vector $1/2 \langle 111 \rangle$ impeded by a high lattice friction [8–11]. Moreover, bending tests performed in HfNbTaTiZr at room temperature suggest that the maximum shear stress plane and the slip plane are identical, indicating frequent cross-slipping [12]. Meanwhile, tensile

tests performed in this alloy above room temperature have shown that the temperature dependence of the yield stress disappears at temperatures above 600–700 K and then serrations appear in stress-strain curves [13–17]. These serrations are compatible with a dynamic strain ageing mechanism, revealing the strong impact of interstitial solutes on the plastic deformation mechanisms, particularly in the high temperature regime where the solutes become mobile. Also, tensile creep tests conducted up to 1600 K suggest a solute drag mechanism in HfNbTaTiZr implying dislocation glide at elevated temperatures [18]. All the above-mentioned deformation mechanisms are consistent with a strong influence of impurities on dislocation glide and on the associated thermally-activated mechanisms in the HfNbTaTiZr alloy. These solute atoms can also impact plasticity by forming enriched complexes. An experimental study [19] reported that oxygen can drive to the formation of nanometric ordered complexes with a local O, Ti and Zr enrichment in HfNbTiZr, leading to an important increase both in yield strength and ductility because of the pinning force exerted by these clusters on dislocations, while no ordered nitrogen-containing complexes are present in the same alloy. DFT calculations have confirmed the chemical preference of O interstitials to bind with Ti and Zr in this alloy [20].

In order to better understand the effects of impurities in solid solution on HfNbTaTiZr plasticity, an atomistic study of the screw dislocation core structure and its interaction with interstitial solutes appears necessary in this alloy. The mechanisms controlling deformation in BCC

* Corresponding author.

E-mail address: emmanuel.clouet@cea.fr (E. Clouet).

¹ Emmanuel Clouet was an Editor of the journal during the review period of the article. To avoid a conflict of interest, Emmanuel Clouet was blinded to the record and another editor processed this manuscript.

RHEA have been addressed through atomistic studies based on density functional theory (DFT), in particular in NbTiZr alloy, where screw dislocations spread on varying planes along their line [21,22]. These complex core structures could be related to the high content of HCP elements present in this alloy. Notably, in the BCC MoNbTaW alloy composed only of BCC elements, screw dislocations maintain a compact core structure [23], which is similar to the case in pure BCC transition metals [24].

The present analysis is grounded on extensive DFT-based investigations of dislocation glide in dilute interstitial solid solutions coupled to *ab initio* simulations, especially in Fe-C and W-C alloys, where it has been shown that the segregation of carbon impurities on screw dislocations leads to a core reconstruction responsible for an important lattice friction opposing their glide at high temperature [25–33]. We therefore examine in the present work if such a core reconstruction induced by the interaction of screw dislocations with interstitial solute impurities also exists in HfNbTaTiZr alloy, partly rationalizing the impact of these impurities on plasticity in this alloy, as mentioned above. First, the bulk behaviour of the HfNbTaTiZr alloy is studied using *ab initio* calculations, focusing on the elastic constants and the dissolution of interstitial solutes, such as carbon, nitrogen and oxygen, in the BCC matrix. The dislocation core structures in presence of these solutes and the associated interaction energies are then determined using *ab initio* and analysed through the effect of the chemical environment.

2. Methods

2.1. DFT calculations

Ab initio calculations are performed using density functional theory (DFT) [34,35] with the Vienna *Ab initio* Simulation Package (VASP) [36]. Pseudopotentials built with the projected-augmented-wave method [37,38] are used with a kinetic energy cutoff of 400 eV. We use pseudopotentials without semicore electrons for Ta, Hf and Ti, with 4p valence states for Nb, and with 4p and 4s valence states for Zr. The exchange–correlation is described by the generalized gradient approximation using the Perdew–Burke–Ernzerhof functional [39]. The Brillouin zone is sampled on a regular grid generated with Monkhorst–Pack scheme and integration is performed with the Methfessel–Paxton approach using a 0.2 eV smearing parameter. Atomic positions are relaxed until all components of the ionic forces are smaller than 10^{-2} eV/Å, while periodicity vectors are kept fixed during relaxation.

2.2. Simulation cells

Different simulation cells are used for the calculation of the alloy elastic constants and for the modelling of dislocations and of their interaction with interstitial solute atoms.

2.2.1. Cell for elastic constants

The elastic constants of the HEA are determined with a periodic BCC unit cell containing 125 atoms using the periodicity vectors $\vec{p}_1 = 5/2[\bar{1}\bar{1}1]$, $\vec{p}_2 = 5/2[1\bar{1}\bar{1}]$, and $\vec{p}_3 = 5/2[111]$. The Brillouin zone is sampled with a $4 \times 4 \times 4$ shifted *k*-point grid. The configuration of the equiatomic HfNbTaTiZr alloy is generated with the special quasirandom structure (SQS) method [40], using the Alloy Theoretic Automated Toolkit (ATAT) package [41]. The alloy configuration is therefore close to random, as expected from a quench from high temperatures. The elastic constants of the pure elements are calculated using the primitive BCC unit cell and a $20 \times 20 \times 20$ shifted *k*-point grid.

2.2.2. Cell for dislocations

Dislocation calculations are performed using the periodicity vectors defined from the elementary vectors $\vec{u}_1 = [\bar{1}\bar{1}2]$, $\vec{u}_2 = [1\bar{1}0]$, and $\vec{u}_3 = 1/2[111]$ (i.e. the dislocation Burgers vector \vec{b}), leading to $\vec{p}_1 = (5\vec{u}_1 - 9\vec{u}_2)/2$, $\vec{p}_2 = (5\vec{u}_1 + 9\vec{u}_2)/2$, and $\vec{p}_3 = 4\vec{u}_3$ as described in Fig. 1. Cells of different heights along the Burgers vector direction with $\vec{p}_3 = 2\vec{b}$, $4\vec{b}$, and $6\vec{b}$ have been tested and the $4\vec{b}$ cell appears to be the minimum size leading to a distribution of chemical species along the $[111]$ direction close enough to random. Indeed atomic relaxations in the smallest $2\vec{b}$ cell lead to crystallographic structures, which can locally strongly differ from the BCC structure. The $4\vec{b}$ height leads to 540 atoms in the simulation cell. A $2 \times 2 \times 4$ shifted *k*-point grid is used to sample the Brillouin zone.

In order to use periodic boundary conditions when modelling dislocations, a dislocation dipole has to be introduced in the simulation cell [24,42]. We use an almost quadrupolar arrangement in order to minimize the elastic interaction between the dislocations and their periodic images. The dislocation dipole is incorporated using anisotropic elasticity theory, taking full account of periodicity. A homogeneous strain is applied to the periodicity vectors of the cell to cancel the plastic strain induced by the dislocation dipole [24,42], thus leading to zero stress calculations. It is then important that both dislocations composing the dipole have exactly the same chemical environment to ensure that they relax towards the same configuration and in order to be able to define without any ambiguity either their core energy or their interaction energy with a foreign solute atom. Some symmetry operations are therefore imposed to the simulation cell although we want to model a random alloy. This is performed by generating a SQS configuration with ATAT for a simulation cell of height $\vec{p}_3/2 = 2\vec{b}$, containing thus 270 atoms. An image of this initial cell is then built by imposing a π rotation around \vec{u}_1 . Both the initial and the image cells are then assembled together to build the final supercell of $4\vec{b}$ height containing 540 atoms, as illustrated in Fig. 1. The resulting supercell has two positions, each defined by a triangle of three neighbouring $[111]$ atomic columns, where the chemical environment is exactly the same. Positioning the dislocation dipole on these two positions guarantees that both dislocations have the same chemical environment. We check that this cell constructed using specific symmetry operations leads to the same atomic relaxation for the two dislocations localized on the two equivalent positions. The same holds for the introduction of two solute atoms on the two equivalent interstitial positions.

2.3. Elastic constants

The elastic constants $C' = (C_{11} - C_{12})/2$ and C_{44} of the random BCC alloy are obtained through a fit of the energy variation when a strain ϵ is applied to the cubic unit cell in the Cartesian coordinate system, \vec{u}_x , \vec{u}_y and \vec{u}_z . A pure shear in the *xz* plane is considered for C_{44} :

$$\begin{pmatrix} 0 & 0 & \epsilon \\ 0 & \frac{\epsilon^2}{1-\epsilon^2} & 0 \\ \epsilon & 0 & 0 \end{pmatrix}, \quad (1)$$

while a traction/compression along *x* axis is considered for C' :

$$\begin{pmatrix} \frac{-\epsilon(2+\epsilon)}{(1+\epsilon)^2} & 0 & 0 \\ 0 & \epsilon & 0 \\ 0 & 0 & \epsilon \end{pmatrix}. \quad (2)$$

These strain tensors are designed to guarantee that they do not induce any volume variation. The bulk modulus $B = (C_{11} + 2C_{12})/3$, is deduced from a hydrostatic dilatation of the cell.

Although the random HEA has the cubic symmetry of its underlying BCC lattice, this is not exactly true for the SQS structure used to model this alloy in the 125-atom supercell. We check that this SQS structure is a good approximation of the truly random alloy by computing the elastic constants for the three different *x*, *y* and *z* traction/compression

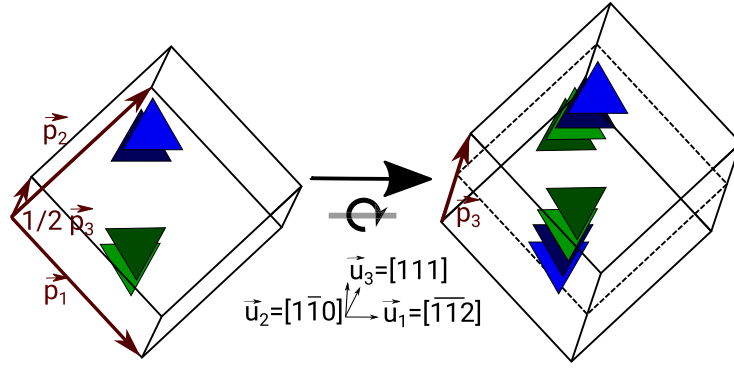


Fig. 1. Schematic illustration of the supercell construction leading to the same chemical environment for both dislocation cores. The initial 270-atom supercell (left) is replicated by imposing a π rotation around \vec{u}_1 . The final 540-atom supercell (right) is obtained by assembling the initial and the image 270-atom supercells along the $[111]$ direction. The triangles defined by the three neighbouring $[111]$ atomic columns belonging to the dislocation cores are sketched in different colours. (For interpretation of the references to colour in this figure legend, the reader is referred to the web version of this article.)

Table 1

Lattice parameters and elastic constants of the five elements composing the alloy in their BCC configuration.

Element	a (Å)	C_{44} (GPa)	C' (GPa)	B (GPa)
Hf	3.531	50	-26	107
Nb	3.324	15	54	174
Ta	3.309	66	50	199
Ti	3.236	35	-5	112
Zr	3.575	36	-5	87

axis orientations and for the three different yz , xz and xy shear planes involved in the calculation of C' and C_{44} , respectively. Close values are expected if the supercell is large enough.

To highlight the importance of atomic relaxations in the HEA, we also consider different relaxation schemes when computing the elastic constants. First, no atomic relaxation is performed (denoted NR for non-relaxed), *i.e.* we consider atoms on a perfect BCC lattice. The second scheme involves partial relaxations (denoted PR), *i.e.* starting from the fully relaxed state, the strain is applied and no further relaxation is performed. Finally, in the full relaxation scheme (denoted FR), the strained cell is fully relaxed. This last scheme leads to the true elastic constants of the alloy.

3. HEA bulk behaviour

3.1. Elastic constants of pure elements

Before studying the elastic behaviour of the HEA, we compute the elastic constants of the five elements composing the HEA in their pure BCC phase at their equilibrium lattice parameter (Table 1).

The BCC structure is the stable phase of niobium and tantalum. Thus all their elastic constants are found positive, in agreement with previous *ab initio* studies [22,43–48]. Hafnium, titanium, and zirconium have an HCP structure at low temperatures and should be unstable in the BCC structure. As a result, their elastic constant C' is negative, indicating a mechanical instability in the corresponding straining direction of the BCC lattice. This agrees with previous *ab initio* calculations [22,46–48]. The most negative value is obtained for hafnium, which is the less stable element in the BCC structure and may therefore destabilize locally the BCC lattice in the HEA. The differences between the lattice parameters of these five elements of up to 0.27 Å may also lead to important relaxations in the HEA.

3.2. Elastic constants of the HEA

The BCC lattice parameter of the HEA is equal to 3.401 Å when the atomic positions are fully relaxed. A very close value is obtained

when the atomic relaxations are neglected, equal to 3.389 Å. Atomic relaxations have therefore an almost negligible impact on the equilibrium lattice parameter. These values are in perfect agreement with experimental lattice parameters in the same equimolar quinary alloy: Stepanov et al. [49] measured 3.40 Å, Chen et al. [50], 3.408 Å, Juan et al. [51], 3.406 Å and Fazakas et al. [52], 3.404 Å. EMTO-CPA calculations [52] lead to a slightly larger value, 3.457 Å.

The elastic constants calculated with the different relaxation schemes are gathered in Table 2. The BCC lattice of the HEA is found to fulfil the mechanical stability criteria ($C_{44} > 0$, $C_{11} + 2C_{12} > 0$ and $C_{11} > C_{12}$). C_{44} and C' are independent of the chosen orientation among the three possible cubic directions with a variation of at most 1 GPa that can be neglected. The 125-atom SQS supercell is therefore large enough to reproduce the cubic symmetry expected for the elastic answer of the random HEA. With an elastic anisotropy ratio $A = C_{44}/C' = 1.6$ much larger than 1, this HEA is found to have a high elastic anisotropy. The elastic constants significantly depend on the relaxation scheme, with C_{44} and C' the most sensitive. Notably, a significant increase in C' is obtained when the atomic positions are fully relaxed, as also evidenced in TaTiHf alloy [53]. Therefore it appears necessary to consider the full atomic relaxations to accurately determine the elastic constants in this HfNbTaTiZr HEA.

Our results are in very good agreement with Ref. [54] also employing VASP but differ from previous *ab initio* calculations based on the EMTO-CPA approach [52]. We see that different values are obtained (Table 2), in particular for the shear modulus C_{44} which is much larger with EMTO-CPA leading to a much higher elastic anisotropy. This discrepancy between VASP and EMTO-CPA calculations cannot be rationalized with a different handling of atomic relaxations. Indeed allowing or not the relaxation in our VASP calculations does not reduce the difference between the two *ab initio* approaches. This difference probably stems from the different description of the electronic structure used in both modelling approaches.

No experimental data exists in the literature for the elastic constants of the single crystal in the HfNbTaTiZr HEA and only polycrystal elastic constants have been measured [51,55,56]. Thus to compare these theoretical values with experiments, it is necessary to perform an averaging procedure. Assuming an isotropic texture, the Hill homogenization approach [57] allows to deduce the isotropic elastic constants of the polycrystal from the anisotropic elastic constants of the single crystal. This leads to an unchanged bulk modulus B and to a shear modulus μ , which is the mean of Voigt μ_V and Reuss μ_R averages, $\mu = (\mu_V + \mu_R)/2$, with:

$$\mu_V = \frac{1}{5}(C_{11} - C_{12} + 3C_{44}),$$

$$\mu_R = 5 \frac{C_{44}(C_{11} - C_{12})}{4C_{44} + 3(C_{11} - C_{12})}.$$

Table 2

Equilibrium lattice parameter a (in Å) and elastic constants (in GPa) of the HEA for different relaxation schemes (NR for non-relaxed, PR for partially relaxed and FR for fully relaxed), and compared to EMTO-CPA calculations [52] and other VASP calculations [54]. The elastic constants C' and C_{44} are determined for three different orientations, which are equivalent in the cubic crystal, and are then averaged.

Method	a	C_{44}			$\langle C_{44} \rangle$	C'			$\langle C' \rangle$	B
		xy	xz	yz		x	y	z		
VASP NR (this work)	3.389	36.5	37.3	36.7	37	15.3	15.3	15.4	15	131
VASP PR (this work)	3.401	45.6	45.8	45.2	46	28.3	28.9	29.7	29	131
VASP FR (this work)	3.401	35.5	35.2	36.7	36	22.0	21.8	24.1	23	123
EMTO-CPA [52]	3.457				62				18	136
VASP [54]	3.40				37				25	125

Table 3

Lattice parameter (in Å) and averaged elastic constants (in GPa) obtained from this work and from EMTO-CPA [52] and VASP calculations [54], and compared to experimental values [51,55,56].

Method	a	B	E	μ
VASP FR (this work)	3.401	123	83	30
EMTO-CPA [52]	3.457	136	104	38
VASP [54]	3.40	125	85	31
Compression tests [51]	3.406		85	
Ultrasound [55]		135	79	28
Resonance [56]		62	90	36

The Young modulus is then simply calculated from the bulk and the shear moduli: $E = 9\mu B / (3B + \mu)$.

The theoretical values we obtain from our VASP calculations are in very good agreement with experimental values of the polycrystal elastic constants determined at room temperature by ultrasound measurements [55], and by compression tests [51]. The comparison with resonance frequency measurements performed during bending and torsion oscillating tests [56] leads to a good agreement for both the Young and the shear moduli, E and μ , but not for the bulk modulus B , with a surprisingly low experimental value (see Table 3).

3.3. Dissolution of C, N and O interstitial solute atoms in the HEA

Before considering dislocations in the HEA and their interaction with foreign interstitial solute atoms, we first characterize the dissolution of these interstitial solutes in the BCC matrix, focusing on carbon, nitrogen and oxygen atoms. Octahedral sites are expected to be the ground state for large interstitial atoms such as C, N, and O, while tetrahedral sites may accommodate smaller atoms such as H and He. We thus insert the interstitial solute atom on the center of gravity of the six neighbouring atoms defining the octahedral site. All *ab initio* calculations are performed in the 540-atom supercell, *i.e.* in the cell used to model dislocations. Two solute atoms are inserted in the simulation cell on the positions that have exactly the same chemical environment (see Section 2.2.2). Two different SQS structures, denoted SQS1 and SQS2, are considered and the solute atoms are inserted in one of the four different layers along the $\langle 111 \rangle$ direction, thus leading to eight different chemical environments for each solute species.

The solution energy of the interstitial atom $X=C, N$ or O is defined as:

$$E_X^{\text{sol}} = \frac{1}{2} [E_{\text{bulk}+2X} - (E_{\text{bulk}} + 2E_X)], \quad (3)$$

where $E_{\text{bulk}+2X}$ and E_{bulk} are the energies of the same supercell respectively with and without the interstitial solute atoms and E_X is the reference state energy of the solute. The chosen reference states are the O_2 molecule, the N_2 molecule, and the diamond structure of carbon, leading to $E_O = 4.39$ eV, $E_N = 8.29$ eV, and $E_C = 9.05$ eV. Solution energies obtained after atomic relaxation are represented as distributions in Fig. 2. Each solute leads to a well separated distribution, with oxygen leading to the most negative values, $E_O^{\text{sol}} = -4.95 \pm 0.43$ eV, then nitrogen with $E_N^{\text{sol}} = -2.90 \pm 0.32$ eV, and finally carbon with $E_C^{\text{sol}} = -1.17 \pm 0.23$ eV. The eight different chemical environments for each

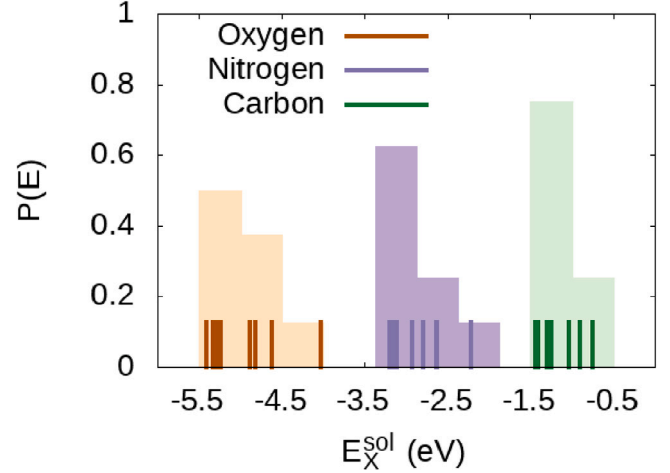


Fig. 2. Distribution of the solution energy (Eq. (3)) for the different solutes. Each impulse corresponds to the result of a single calculation. A total of eight different configurations per solute are considered. The histograms are obtained by grouping the obtained energies using a bin width equal to 0.5 eV.

solute atom lead to valuable results, although many more additional configurations would be required to obtain well-converged distributions describing quantitatively the interaction of interstitial elements with the HEA matrix. Nevertheless, this study gives general trends and well-distinct distributions between the three different solutes. Oxygen appears therefore as the chemical element the most prone to dissolution in this HEA.

4. Screw dislocation

4.1. Core structure in the HEA

We now investigate the structure of the screw dislocation core in the equimolar HEA using the 4b simulation cell containing 540 atoms. The dislocation dipole is introduced in the relaxed BCC bulk cell on positions corresponding to easy cores, *i.e.* the known ground state in pure BCC metals [24]. Atomic relaxations lead to a non-compact core, with the dislocation spreading in different planes along its line and with the core delocalized on several atomic columns as shown in Fig. 3. This non-compact core is obtained for the two chemical configurations corresponding to the two different investigated SQS structures, SQS1 and SQS2. For one of this structure, SQS2, we also start from a configuration corresponding to a hard core by keeping the same initial positions for the centers of the two dislocations composing the dipole in their easy core configurations and by inverting their Burgers vector. Relaxation still leads to non-compact cores with a varying spreading along the dislocation line. Previous *ab initio* calculations [22,54], as well as simulations with empirical potentials [21], have evidenced similar non-compact dislocation cores in the HfNbTaTiZr alloy and similar variation of the core spreading along the dislocation line in the ternary NbTiZr and Nb₁₇Ti₃₃Zr₅₀ alloys but not in Nb₅₀Ti₃₃Zr₁₇ where the

screw dislocation is shown to keep its compact core. The core spreading obtained here may be induced by the high content of HCP elements (Ti, Zr, Hf) considered in the HfNbTaTiZr alloy. Indeed *ab initio* calculations in the MoNbTaW and MoNbTaVW equimolar alloys [23,54], two HEA with only BCC elements, lead both to compact cores for the screw dislocation. This non-compact core evidenced in HfNbTaTiZr could explain the lattice friction, which is observed experimentally when screw dislocations glide in this alloy [8,10,11]. As it does not belong to any particular slip plane, it can easily cross-slip, in agreement with experimental observations in this HfNbTaTiZr alloy [12].

We extract the core energy from the three obtained dislocation configurations (SQS1 and SQS2 structures with initial easy core configuration and SQS2 with initial hard core configuration), using the methodology proposed in Ref. [58]:

$$E^{\text{core}} = \frac{1}{2h} [E_{2D} - E_{\text{bulk}} - E^{\text{elas}}], \quad (4)$$

where $h = 4b$ is the height of the cell, E_{2D} is the energy of the cell containing the dislocation dipole, and E^{elas} is the elastic energy of the cell. This elastic energy is calculated using the elastic constants of the alloy, determined in Section 3.2, using anisotropic elasticity and taking full account of periodic boundaries [42]. This leads to an elastic energy of 3.70 eV in the $4b$ cell and for a core cutoff radius $r_c = b$. The resulting core energies of the three investigated configurations are then equal to 44, 118, and 78 meV/Å. These values are comparable to the ones obtained in the pure BCC metals with the same core cutoff radius, i.e. in Nb and Ta (respectively 171 meV/Å and 153 meV/Å [59]).

4.2. Dislocation interaction with C, N and O interstitial solute atoms

We now examine the interaction of the screw dislocation with an interstitial solute atom, considering C, N and O atoms. Solute atoms are inserted in an octahedral interstitial site of the relaxed dislocation structure, in a position corresponding to a first nearest neighbour interstitial site of the initial dislocation core position. As the relaxed core is not localized anymore, one cannot clearly define the dislocation-solute relative position. For the same solute position in the (111) plane, we investigate the four different octahedral sites existing along the [111] direction in the two SQS structures, leading thus to eight different chemical environments for each solute. After relaxation, the dislocation keeps a non-compact core spread on several atomic columns, with the core tending to move away from the interstitial atom, which stays in its initial octahedral site. This is illustrated in Fig. 4a showing the relaxed structure after the insertion of an oxygen atom. Comparing with the relaxed structure in absence of a solute atom (first row and first column of Fig. 3 corresponding to SQS1 for $0 < z < b$), one can see that the oxygen atom repels the dislocation. The tendency for the dislocation to move away from the solute atom is observed with the three different solutes.

Ab initio calculations in pure BCC metals have shown that interstitial solute atoms, in particular carbon, induce a core reconstruction with the dislocation adopting a hard core configuration and the solute atom relaxing towards the prismatic core site [27,29,31–33,60]. Thus we examine the possibility for this prismatic configuration to be also stable in the HfNbTaTiZr alloy. We start from an unrelaxed dislocation core in a hard core configuration and we insert the solute atom in the prismatic core site. Calculations are performed for the two SQS structures, considering the four possible insertion sites for the solute along the dislocation line, thus leading to eight additional configurations for each solute. Two different types of configuration are obtained upon relaxation. In most cases, the solute moves back into a neighbouring octahedral site and the dislocation spreads in several atomic columns (Fig. 4b), leading thus to a configuration similar to the one previously obtained starting from an easy core position. A different configuration is observed only in the case of oxygen for two of the eight calculations, with the oxygen atom staying in the prismatic core site and the dislocation center

remaining on a hard core with some spreading on the neighbouring [111] columns (Fig. 4c).

In presence of an interstitial solute atom, the screw dislocation in HfNbTaTiZr alloy remains spread on several planes, with a varying spreading along the dislocation line. This behaviour is different from pure BCC metals, where the solute - dislocation interaction leads to a core reconstruction which remains compact. While dynamic strain ageing is observed both in HfNbTaTiZr alloy [13–17] and in pure BCC metals, some differences in the underlying mechanisms can be inferred from the different behaviours revealed by *ab initio* calculations. The attractive interaction observed for some solute positions with the screw dislocation would lead to the formation of Cottrell atmospheres around dislocations at high enough temperatures, causing a glide motion controlled by pinning and unpinning of the dislocation at intermediate temperature, and a viscous glide of the dislocation with its solute atmosphere at the highest temperature. This classical picture of the dynamic strain ageing is independent of the dislocation character and should operate in the HfNbTaTiZr alloy like in other BCC metals and alloys. But one does not expect to observe in the HfNbTaTiZr alloy the reappearance of a large lattice friction on screw dislocations at high temperatures, leading to a reduced mobility of the screw dislocations compared to other orientations, as it has been observed in pure Fe [25,26,30] and pure W [28] in presence of carbon atoms. Indeed, this reappearance of a Peierls mechanism at high temperature in Fe and W results from the strong attraction of screw dislocations with interstitial solute atoms, leading to their transformation and their pinning in a reconstructed core configurations. Our *ab initio* calculations therefore predict a difference between HfNbTaTiZr alloys and pure BCC metals in the dislocation mobility in the regime where diffusion of interstitial solute atoms is fast enough to allow for their segregation on dislocations.

The interaction energy between the dislocation and the solute is defined by:

$$E_{D-X}^{\text{inter}} = \frac{1}{2} [E_{2D+2X} - \langle E_{\text{bulk}+2X} \rangle - \langle E_{2D} \rangle + \langle E_{\text{bulk}} \rangle], \quad (5)$$

where E_{2D+2X} is the energy of the cell containing a dislocation dipole and two solute atoms. Here $\langle E_{2D} \rangle$ and $\langle E_{\text{bulk}} \rangle$ are the average values over the two SQS configurations of respectively E_{2D} (where the dislocations are initially in easy core configurations) and E_{bulk} . $\langle E_{\text{bulk}+2X} \rangle$ is the average value of $E_{\text{bulk}+2X}$ over the eight different chemical environments for a given species X. With this definition, a positive interaction energy means a repulsive interaction.

The interaction energies obtained for each solute in the sixteen different chemical environments are gathered in Fig. 5. According to the energy distributions, the three interstitial solute atoms exhibit almost a similar range of interaction energies, between –1 eV (strongly attractive) and 0.5 eV (repulsive). The case of oxygen leads to two values which are greater than 0.5 eV and thus out of this range. One of these values (0.63 eV) corresponds to a spread core without any significant difference from the configurations obtained for oxygen in other chemical environments. The corresponding relaxed configuration is the same as the one obtained for nitrogen or carbon. The only specificity of this configuration is that five of the six metal atoms defining the octahedral site of oxygen are elements with a BCC ground state (Nb or Ta). As it will be shown below, such a configuration is more repulsive in the case of oxygen than in the case of nitrogen or carbon. The second value (0.78 eV) corresponds to the most repulsive interaction and the associated relaxed configuration is a reconstructed core, where the dislocation remains in a hard core configuration and where the oxygen atom lies in its initial prismatic core site. Another configuration where the dislocation remains in a hard core structure with oxygen in a prismatic core site is also evidenced, associated to a repulsive interaction energy (0.30 eV) although the repulsion is weaker. In conclusion, although such a reconstructed core can be stabilized by an oxygen atom, the two configurations previously described lead to repulsive interactions between the dislocation and the oxygen atom,

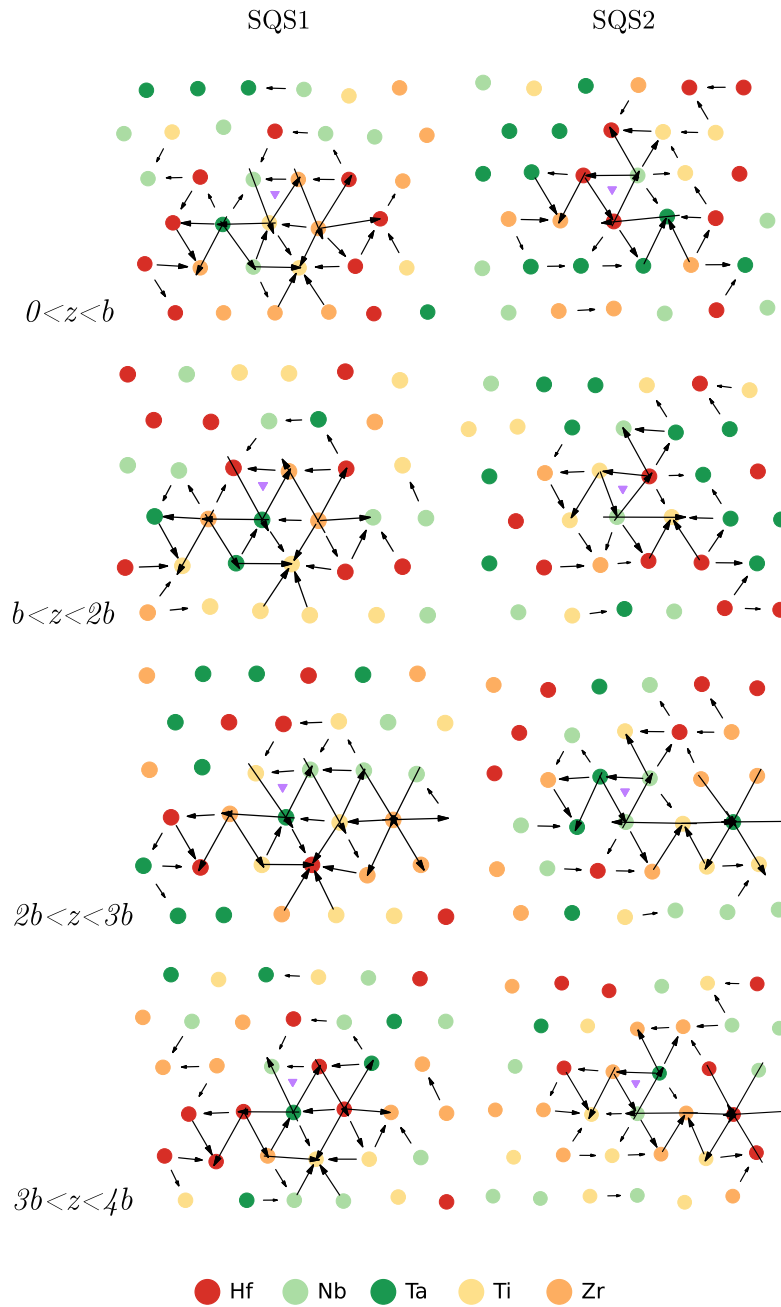


Fig. 3. Differential displacement map showing the dislocation core in the four layers along [111] for the two chemical configurations, SQS1 (left) and SQS2 (right). The atomic structure is projected in the (111) plane perpendicular to the dislocation line. Relaxed atomic positions are drawn as circles with a colour according to their chemical nature. The purple triangle represents the initial position of the dislocation on an easy core configuration. (For interpretation of the references to colour in this figure legend, the reader is referred to the web version of this article.)

indicating that these configurations are not energetically favourable. These energy distributions lead to the following average interaction energies: $E_{\text{D-O}}^{\text{inter}} = -0.18 \pm 0.48$ eV, $E_{\text{D-C}}^{\text{inter}} = -0.22 \pm 0.23$ eV, and $E_{\text{D-N}}^{\text{inter}} = -0.25 \pm 0.32$ eV. To improve the statistic convergence, more random chemical environments for the interstitial atoms could be considered. However this should not change the overall conclusion that the interaction energies between the dislocation and the interstitial atom are attractive in average for the three solutes considered.

To better understand the dispersion of the interaction energy, we analyse the structural and chemical environments of the foreign solute atoms in each configuration. We first investigate the geometry of the interstitial site by computing the interatomic distance between the solute and its six nearest neighbours. The calculation is executed for each solute in the sixteen chemical environments with and without

dislocation. Note that even in the hard core configuration stabilized by the presence of oxygen, this calculation is possible. In this case, the six metallic atoms form a trigonal prism and are all first nearest neighbours of the oxygen atom sitting in the prismatic site. To understand the impact of the solute atom, we also compute the same interatomic distance in the empty octahedral site by determining the isobarycenter of the same six metallic atoms before adding the solute atom and then by calculating the distance of the six metallic atoms from the isobarycenter. The results of this analysis are gathered in Fig. 6. For all solutes, we evidence a distortion of the octahedral site induced by the presence of the interstitial atom, which no longer allows us to distinguish the first and second nearest neighbours of the solute atom. The average distance between the solute atom and its six neighbours is 2.2 Å for all solutes. In comparison, the octahedral site in perfect

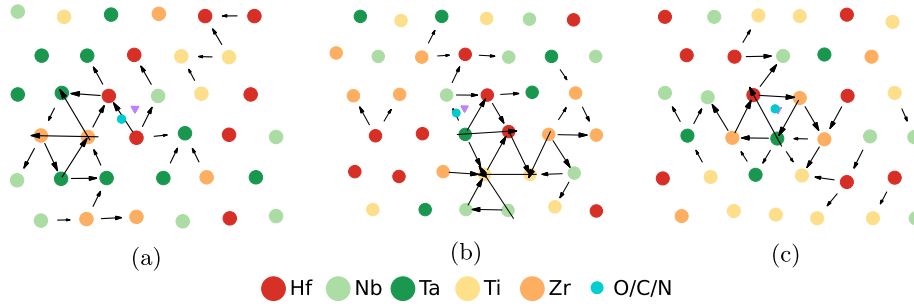


Fig. 4. Differential displacement map showing the relaxed structure of a screw dislocation interacting with an interstitial solute atom (blue point) for three different configurations. The represented layer is the one containing the solute atom. The initial configuration (represented by a purple triangle) corresponds to (a) an easy core and (b,c) a hard core. In (c), the dislocation remains in its hard core structure with the solute atom staying in a prismatic core site. (For interpretation of the references to colour in this figure legend, the reader is referred to the web version of this article.)

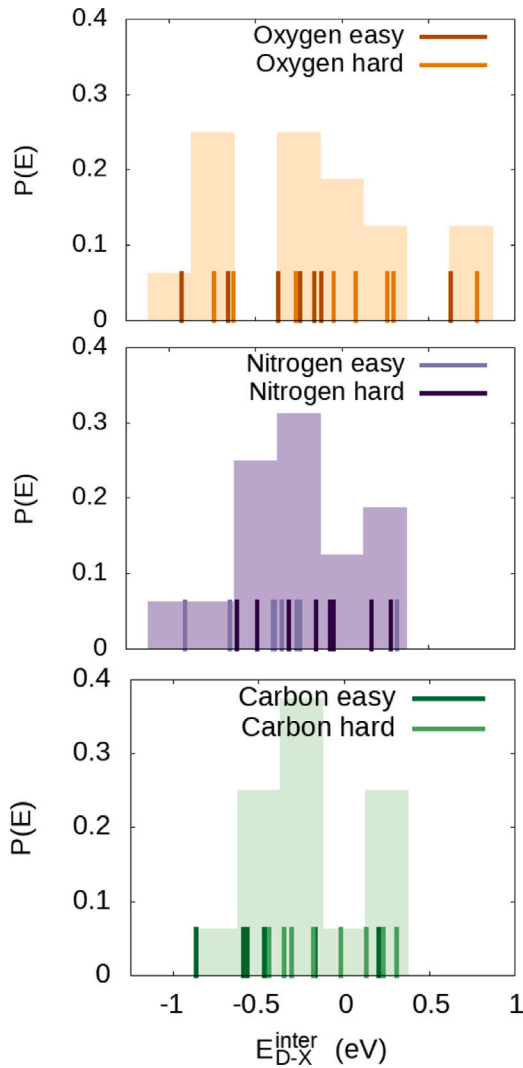


Fig. 5. Distributions of the interaction energies between a solute and a screw dislocation. Each impulse corresponds to the result of a single calculation. In total eight configurations starting from a relaxed easy core and eight additional ones starting from an unrelaxed hard core are investigated. The histograms are obtained by grouping the obtained energies using a bin width equal to 0.25 eV.

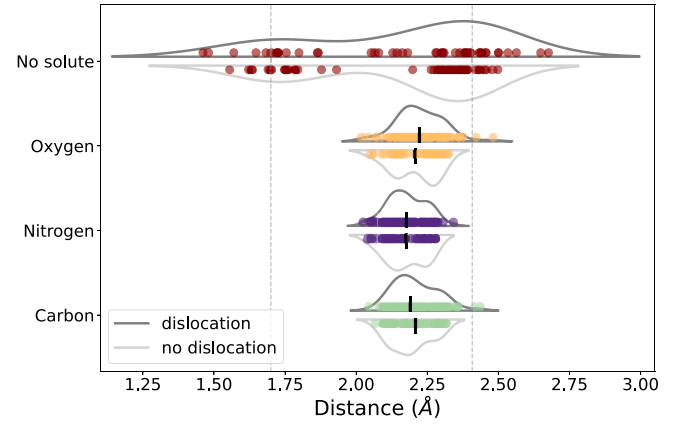


Fig. 6. Interatomic distance (in Å) between the solute and its six nearest neighbours in the bulk (on bottom) and in the vicinity of the dislocation (on top) for each of the three interstitial atoms. Each point corresponds to one neighbouring metallic atom. The density of the interatomic distance (calculated using the Kernel density estimation) is also plotted in dark grey for the configuration with dislocation and in light grey without dislocation. For each of the three solutes, the black bar represents the average distance between the interstitial atom and its six nearest neighbours. The interatomic distances for the configurations without any solute are also plotted for comparison. The interatomic distances in the configurations containing dislocations take into account the sixteen different chemical environments (*i.e.* the hard and easy cores in SQS1 and SQS2 structures) whereas the distances in the configurations without dislocation consider eight different chemical environments (*i.e.* SQS1 and SQS2 structures).

bulk is located at a distance $a/2 = 1.7 \text{ Å}$ from its first two nearest neighbours and $a/\sqrt{2} = 2.4 \text{ Å}$ from its four second nearest neighbours. The structures without solute display two poles representing the two different types of neighbours (first and second nearest neighbours) situated around these ideal bulk values. The fact that the three average interatomic distances for the three solutes are close means that there is no effect of the chemical nature of the solute. We also note that the presence of the dislocation does not impact the distortion of the octahedral site since the same interatomic distance of around 2.2 Å is obtained with and without the dislocation (Fig. 6).

After studying the geometrical structure of the interstitial site occupied by the solute atom, we look at the chemical nature of the six metallic atoms defining either the octahedral or the prismatic site where the solute sits. We count around the solute the number of elements with a BCC ground state, denoted N_{BCC} , (Nb, Ta) and the number of elements with an HCP ground state (Hf, Ti, Zr). When starting from a dislocation in an easy core structure, all solutes remains in the same octahedral site defined by their initial positions, thus leading to the same chemical environments for oxygen, carbon or nitrogen. This is not necessary the case when starting from a hard core structure, as the solute, initially in a prismatic site, may either stay in this prismatic

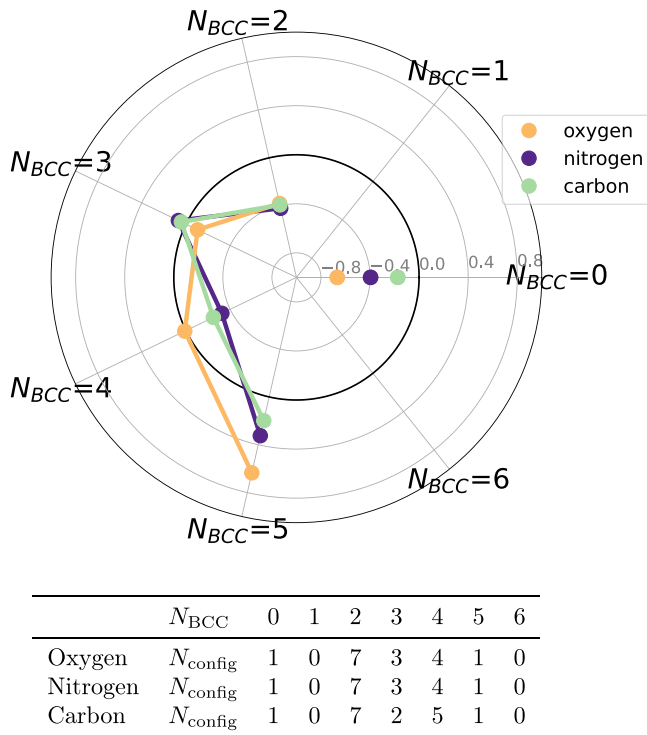


Fig. 7. Average interaction energy as a function of the number N_{BCC} of BCC elements in the direct vicinity of the solute in an octahedral or prismatic position. The table gives the number N_{config} of different chemical environments for each value of N_{BCC} and each solute.

site or relax to a different octahedral site, depending of the type of the solute atom. This results in different chemical environments amongst the solutes for a given initial configuration, as shown in the table of Fig. 7. We then plot the interaction energy as a function of N_{BCC} , which can vary from 0 to 6 (Fig. 7). The analysis is limited by the low statistics obtained with only sixteen different configurations per solute, for which the interstitial atom is mostly surrounded by HCP elements and that are unevenly distributed amongst all possible arrangements (Fig. 7). However, one can draw general trends. Notably the dislocation-solute interaction energy is more attractive when the solute atom is surrounded only by HCP elements ($N_{BCC} = 0$) and tends to increase with N_{BCC} , until it becomes repulsive. This variation is more pronounced for oxygen than for nitrogen or carbon. But, as the interaction energy is defined with respect to average reference states (Eq. (5)), it mainly reflects the fact that oxygen atoms prefer to be surrounded by HCP elements. This particular behaviour of O, which has been shown in pristine crystals [19,20,61,62], remains true in presence of a dislocation.

5. Conclusion

In conclusion, atomistic simulations show that screw dislocations have a non compact core in the BCC HfNbTiTaZr, with a spreading over several [111] atomic columns. Their interaction with interstitial solute atoms like oxygen, carbon and nitrogen is mostly attractive. But contrary to screw dislocations in pure BCC metals, this attractive interaction does not lead to any core reconstruction: the dislocation displays a similar spreading in presence or absence of a solute atom and the solute atom stays in an octahedral site, which shows a similar distortion in the dislocated or pristine crystal. This attraction between screw dislocations and interstitial solute atoms is characterized by an important average interaction energy, between -0.18 and -0.25 eV, depending on the solute element, and a large dispersion. Part of this

dispersion can be rationalized by the chemical environment of the solute atom in its octahedral site, the octahedral sites formed by a large number of HCP elements (Hf, Ti, and Zr) leading to the strongest attraction.

This attractive interaction between interstitial impurities and screw dislocations is consistent with experiments, showing the existence of dynamic strain ageing in this HfNbTiTaZr alloy at high enough temperature and a major impact of impurities on plasticity [13–16]. Although a strong interaction of impurities with edge dislocations is also expected, our study clearly shows that the interaction with screw dislocations is important and has to be accounted for to understand plasticity in this alloy.

CRediT authorship contribution statement

Thomas Leveau: Investigation, Writing – original draft, Writing – review & editing. **Lisa Ventelon:** Funding acquisition, Supervision, Writing – original draft, Writing – review & editing. **Emmanuel Clouet:** Supervision, Writing – original draft, Writing – review & editing.

Declaration of competing interest

The authors declare that they have no known competing financial interests or personal relationships that could have appeared to influence the work reported in this paper.

Acknowledgements

We acknowledge the EuroHPC Joint Undertaking for awarding the project ISISHEA access to the EuroHPC supercomputer LUMI, hosted by CSC (Finland) and the LUMI consortium through a EuroHPC Regular Access call. The authors also acknowledge Jean-Philippe Couzinié from ICMPE - CNRS for fruitful discussions on experimental observations in this alloy and, more generally, on plasticity in RHEA.

References

- [1] B. Cantor, I.T.H. Chang, P. Knight, A.J.B. Vincent, Microstructural development in equiatomic multicomponent alloys, *Mater. Sci. Eng. A* 375–377 (2004) 213–218, <http://dx.doi.org/10.1016/j.msea.2003.10.257>.
- [2] J.-W. Yeh, S.-K. Chen, S.-J. Lin, J.-Y. Gan, T.-S. Chin, T.-T. Shun, C.-H. Tsau, S.-Y. Chang, Nanostructured high-entropy alloys with multiple principal elements: Novel alloy design concepts and outcomes, *Adv. Eng. Mater.* 6 (2004) 299–303, <http://dx.doi.org/10.1002/adem.200300567>.
- [3] O. Senkov, G. Wilks, D. Miracle, C. Chuang, P. Liaw, Refractory high-entropy alloys, *Intermetallics* 18 (2010) 1758–1765, <http://dx.doi.org/10.1016/j.intermet.2010.05.014>.
- [4] O. Senkov, J. Scott, S. Senkova, D. Miracle, C. Woodward, Microstructure and room temperature properties of a high-entropy TaNbHfZrTi alloy, *J. Alloys Compd.* 509 (2011) 6043–6048, <http://dx.doi.org/10.1016/j.jallcom.2011.02.171>.
- [5] O.N. Senkov, D.B. Miracle, K.J. Chaput, J.-P. Couzinié, Development and exploration of refractory high entropy alloys — a review, *J. Mater. Res.* 33 (2018) 3092–3128, <http://dx.doi.org/10.1557/jmr.2018.153>.
- [6] O.N. Senkov, S. Gorsse, D.B. Miracle, High temperature strength of refractory complex concentrated alloys, *Acta Mater.* 175 (2019) 394–405, <http://dx.doi.org/10.1016/j.actamat.2019.06.032>.
- [7] D. Miracle, O. Senkov, A critical review of high entropy alloys and related concepts, *Acta Mater.* 122 (2017) 448–511, <http://dx.doi.org/10.1016/j.actamat.2016.08.081>.
- [8] G. Dirras, J. Gubicza, A. Heczal, L. Liliensten, J.-P. Couzinié, L. Perrière, I. Guillot, A. Hocini, Microstructural investigation of plastically deformed $\text{Ti}_{20}\text{Zr}_{20}\text{Hf}_{20}\text{Nb}_{20}\text{Ta}_{20}$ high entropy alloy by X-ray diffraction and transmission electron microscopy, *Mater. Charact.* 108 (2015) 1–7, <http://dx.doi.org/10.1016/j.matchar.2015.08.007>.
- [9] R.R. Eleti, N. Stepanov, N. Yurchenko, D. Klimenko, S. Zhrebtssov, Plastic deformation of solid-solution strengthened Hf-Nb-Ta-Ti-Zr body-centered cubic medium/high-entropy alloys, *Scr. Mater.* 200 (2021) 113927, <http://dx.doi.org/10.1016/j.scriptamat.2021.113927>.
- [10] J.-P. Couzinié, L. Liliensten, Y. Champion, G. Dirras, L. Perrière, I. Guillot, On the room temperature deformation mechanisms of a TiZrHfNbTa refractory high-entropy alloy, *Mater. Sci. Eng. A* 645 (2015) 255–263, <http://dx.doi.org/10.1016/j.msea.2015.08.024>.

- [11] L. Liliensten, J.-P. Couzinié, L. Perrière, A. Hocini, C. Keller, G. Dirras, I. Guillot, Study of a bcc multi-principal element alloy: Tensile and simple shear properties and underlying deformation mechanisms, *Acta Mater.* 142 (2018) 131–141, <http://dx.doi.org/10.1016/j.actamat.2017.09.062>.
- [12] M. Tanaka, S. Okajo, S. Yamasaki, T. Morikawa, Persistent slip observed in TiZrNbHfTa: A body-centered high-entropy cubic alloy, *Scr. Mater.* 200 (2021) 113895, <http://dx.doi.org/10.1016/j.scriptamat.2021.113895>.
- [13] M. Tanaka, S. Yamasaki, T. Morikawa, Temperature dependence of the yield stress in TiZrNbHfTa body-centered cubic high-entropy alloy, *Mater. Sci. Eng. A* 871 (2023) 144917, <http://dx.doi.org/10.1016/j.msea.2023.144917>.
- [14] S. Chen, W. Li, F. Meng, Y. Tong, H. Zhang, K.-K. Tseng, J.-W. Yeh, Y. Ren, F. Xu, Z. Wu, P.K. Liaw, On temperature and strain-rate dependence of flow serration in HfNbTaTiZr high-entropy alloy, *Scr. Mater.* 200 (2021) 113919, <http://dx.doi.org/10.1016/j.scriptamat.2021.113919>.
- [15] W.-C. Hsu, T.-E. Shen, Y.-C. Liang, J.-W. Yeh, C.-W. Tsai, In situ analysis of the Portevin-Le Chatelier effect from low to high-entropy alloy in equal HfNbTaTiZr system, *Acta Mater.* 253 (2023) 118981, <http://dx.doi.org/10.1016/j.actamat.2023.118981>.
- [16] S.Y. Chen, L. Wang, W.D. Li, Y. Tong, K.K. Tseng, C.W. Tsai, J.W. Yeh, Y. Ren, W. Guo, J.D. Poplawsky, P.K. Liaw, Peierls barrier characteristic and anomalous strain hardening provoked by dynamic-strain-aging strengthening in a body-centered-cubic high-entropy alloy, *Mater. Res. Lett.* 7 (2019) 475–481, <http://dx.doi.org/10.1080/21663831.2019.1658233>.
- [17] H. Chen, T. Hanemann, S. Seils, D. Schliephake, A.S. Tirunilai, M. Heilmaier, K.-P. Weiss, A. Kauffmann, Influence of temperature and plastic strain on deformation mechanisms and kink band formation in homogenized HfNbTaTiZr, *Crystals* 11 (2021) 81, <http://dx.doi.org/10.3390/cryst11020081>.
- [18] C.-J. Liu, C. Gadelmeier, S.-L. Lu, J.-W. Yeh, H.-W. Yen, S. Gorsse, U. Glatzel, A.-C. Yeh, Tensile creep behavior of HfNbTaTiZr refractory high entropy alloy at elevated temperatures, *Acta Mater.* 237 (2022) 118188, <http://dx.doi.org/10.1016/j.actamat.2022.118188>.
- [19] Z. Lei, X. Liu, Y. Wu, H. Wang, S. Jiang, S. Wang, X. Hui, Y. Wu, B. Gault, P. Kontis, D. Raabe, L. Gu, Q. Zhang, H. Chen, H. Wang, J. Liu, K. An, Q. Zeng, T.-G. Nieh, Z. Lu, Enhanced strength and ductility in a high-entropy alloy via ordered oxygen complexes, *Nature* 563 (2018) 546–550, <http://dx.doi.org/10.1038/s41586-018-0685-y>.
- [20] B. Zhang, J. Ding, E. Ma, Chemical short-range order in body-centered-cubic TiZrHfNb high-entropy alloys, *Appl. Phys. Lett.* 119 (2021) 201908, <http://dx.doi.org/10.1063/5.0069417>.
- [21] S.I. Rao, B. Akdim, E. Antillon, C. Woodward, T.A. Parthasarathy, O.N. Senkov, Modeling solution hardening in BCC refractory complex concentrated alloys: NbTiZr, Nb_{1.5}TiZr_{0.5} and Nb_{0.5}TiZr_{1.5}, *Acta Mater.* 168 (2019) 222–236, <http://dx.doi.org/10.1016/j.actamat.2019.02.013>.
- [22] B. Akdim, C. Woodward, S. Rao, E. Antillon, Predicting core structure variations and spontaneous partial kink formation for 1/2<111> screw dislocations in three BCC NbTiZr alloys, *Scr. Mater.* 199 (2021) 113834, <http://dx.doi.org/10.1016/j.scriptamat.2021.113834>.
- [23] S. Yin, J. Ding, M. Asta, R.O. Ritchie, Ab initio modeling of the energy landscape for screw dislocations in body-centered cubic high-entropy alloys, *Npj Comput. Mater.* 6 (2020) 110, <http://dx.doi.org/10.1038/s41524-020-00377-5>.
- [24] D. Rodney, L. Ventelon, E. Clouet, L. Pizzagalli, F. Willaime, Ab initio modeling of dislocation core properties in metals and semiconductors, *Acta Mater.* 124 (2017) 633–659, <http://dx.doi.org/10.1016/j.actamat.2016.09.049>.
- [25] D. Caillard, Dynamic strain ageing in iron alloys: The shielding effect of carbon, *Acta Mater.* 112 (2016) 273–284, <http://dx.doi.org/10.1016/j.actamat.2016.04.018>.
- [26] D. Caillard, J. Bonnevillie, Dynamic strain aging caused by a new Peierls mechanism at high-temperature in iron, *Scr. Mater.* 95 (2015) 15–18, <http://dx.doi.org/10.1016/j.scriptamat.2014.09.019>.
- [27] G. Hachet, L. Ventelon, F. Willaime, E. Clouet, Screw dislocation-carbon interaction in BCC tungsten: an ab initio study, *Acta Mater.* 200 (2020) 481–489, <http://dx.doi.org/10.1016/j.actamat.2020.09.014>.
- [28] G. Hachet, D. Caillard, L. Ventelon, E. Clouet, Mobility of screw dislocation in BCC tungsten at high temperature in presence of carbon, *Acta Mater.* 222 (2022) 117440, <http://dx.doi.org/10.1016/j.actamat.2021.117440>.
- [29] L. Ventelon, B. Lüthi, E. Clouet, L. Provillie, B. Legrand, D. Rodney, F. Willaime, Dislocation core reconstruction induced by carbon segregation in bcc iron, *Phys. Rev. B* 91 (2015) 220102, <http://dx.doi.org/10.1103/physrevb.91.220102>.
- [30] L. Ventelon, D. Caillard, B. Lüthi, E. Clouet, D. Rodney, F. Willaime, Mobility of carbon-decorated screw dislocations in bcc iron, *Acta Mater.* 247 (2023) 118716, <http://dx.doi.org/10.1016/j.actamat.2023.118716>.
- [31] B. Lüthi, L. Ventelon, C. Elsässer, D. Rodney, F. Willaime, First principles investigation of carbon-screw dislocation interactions in body-centered cubic metals, *Modelling Simul. Mater. Sci. Eng.* 25 (2017) 084001, <http://dx.doi.org/10.1088/1361-651x/aa88eb>.
- [32] B. Lüthi, L. Ventelon, D. Rodney, F. Willaime, Attractive interaction between interstitial solutes and screw dislocations in bcc iron from first principles, *Comput. Mater. Sci.* 148 (2018) 21–26, <http://dx.doi.org/10.1016/j.commatsci.2018.02.016>.
- [33] A. Bakaev, A. Zinovev, D. Terentyev, G. Bonny, C. Yin, N. Castin, Y.A. Mastrikov, E.E. Zhurkin, Interaction of carbon with microstructural defects in a W-Re matrix: An ab initio assessment, *J. Appl. Phys.* 126 (2019) 075110, <http://dx.doi.org/10.1063/1.5094441>.
- [34] P. Hohenberg, W. Kohn, Inhomogeneous electron gas, *Phys. Rev.* 136 (1964) B864–B871, <http://dx.doi.org/10.1103/physrev.136.b864>.
- [35] W. Kohn, L.J. Sham, Self-consistent equations including exchange and correlation effects, *Phys. Rev.* 140 (1965) A1133–A1138, <http://dx.doi.org/10.1103/physrev.140.a1133>.
- [36] G. Kresse, J. Furthmüller, Efficient iterative schemes for ab initio total-energy calculations using a plane-wave basis set, *Phys. Rev. B* 54 (1996) 11169–11186, <http://dx.doi.org/10.1103/physrevb.54.11169>.
- [37] P.E. Blöchl, Projector augmented-wave method, *Phys. Rev. B* 50 (1994) 17953–17979, <http://dx.doi.org/10.1103/physrevb.50.17953>.
- [38] G. Kresse, D. Joubert, From ultrasoft pseudopotentials to the projector augmented-wave method, *Phys. Rev. B* 59 (1999) 1758–1775, <http://dx.doi.org/10.1103/physrevb.59.1758>.
- [39] J.P. Perdew, K. Burke, M. Ernzerhof, Generalized gradient approximation made simple, *Phys. Rev. Lett.* 77 (1996) 3865–3868, <http://dx.doi.org/10.1103/physrevlett.77.3865>.
- [40] A. Zunger, S.-H. Wei, L. Ferreira, J. Bernard, Special quasirandom structures, *Phys. Rev. Lett.* 65 (1990) 353–356, <http://dx.doi.org/10.1103/physrevlett.65.353>.
- [41] A. Van De Walle, P. Tiwary, M. De Jong, D. Olmsted, M. Asta, A. Dick, D. Shin, Y. Wang, L.-Q. Chen, Z.-K. Liu, Efficient stochastic generation of special quasirandom structures, *CALPHAD* 42 (2013) 13–18, <http://dx.doi.org/10.1016/j.calphad.2013.06.006>.
- [42] E. Clouet, Ab initio models of dislocations, in: W. Andreoni, S. Yip (Eds.), *Handbook of Materials Modeling*, Springer International Publishing, Cham, 2020, pp. 1503–1524, http://dx.doi.org/10.1007/978-3-319-44677-6_22.
- [43] C.R. Weinberger, G.J. Tucker, S.M. Foiles, Peierls potential of screw dislocations in bcc transition metals: Predictions from density functional theory, *Phys. Rev. B* 87 (2013) 054114, <http://dx.doi.org/10.1103/PhysRevB.87.054114>.
- [44] L. Dezerald, L. Ventelon, E. Clouet, C. Denoual, D. Rodney, F. Willaime, Ab initio modeling of the two-dimensional energy landscape of screw dislocations in bcc transition metals, *Phys. Rev. B* 89 (2014) 024104, <http://dx.doi.org/10.1103/physrevb.89.024104>.
- [45] M. Cottura, E. Clouet, Solubility in Zr-Nb alloys from first-principles, *Acta Mater.* 144 (2018) 21–30, <http://dx.doi.org/10.1016/j.actamat.2017.10.035>.
- [46] H. Ikehata, N. Nagasako, T. Furuta, A. Fukumoto, K. Miwa, T. Saito, First-principles calculations for development of low elastic modulus Ti alloys, *Phys. Rev. B* 70 (2004) 174113, <http://dx.doi.org/10.1103/physrevb.70.174113>.
- [47] S.L. Shang, A. Saengdeejing, Z.G. Mei, D.E. Kim, H. Zhang, S. Ganeshan, Y. Wang, Z.K. Liu, First-principles calculations of pure elements: Equations of state and elastic stiffness constants, *Comput. Mater. Sci.* 48 (2010) 813–826, <http://dx.doi.org/10.1016/j.commatsci.2010.03.041>.
- [48] M. Liao, Y. Liu, P. Cui, N. Qu, F. Zhou, D. Yang, T. Han, Z. Lai, J. Zhu, Modeling of alloying effect on elastic properties in BCC Nb-Ti-V-Zr solid solution: From unary to quaternary, *Comput. Mater. Sci.* 172 (2020) 109289, <http://dx.doi.org/10.1016/j.commatsci.2019.109289>.
- [49] N.D. Stepanov, N.Y. Yurchenko, S.V. Zherebtsov, M.A. Tikhonovsky, G.A. Salishchev, Aging behavior of the HfNbTaTiZr high entropy alloy, *Mater. Lett.* 211 (2018) 87–90, <http://dx.doi.org/10.1016/j.matlet.2017.09.094>.
- [50] S.Y. Chen, Y. Tong, K.-K. Tseng, J.-W. Yeh, J.D. Poplawsky, J.G. Wen, M.C. Gao, G. Kim, W. Chen, Y. Ren, R. Feng, W.D. Li, P.K. Liaw, Phase transformations of HfNbTaTiZr high-entropy alloy at intermediate temperatures, *Scr. Mater.* 158 (2019) 50–56, <http://dx.doi.org/10.1016/j.scriptamat.2018.08.032>.
- [51] C.-C. Juan, K.-K. Tseng, W.-L. Hsu, M.-H. Tsai, C.-W. Tsai, C.-M. Lin, S.-K. Chen, S.-J. Lin, J.-W. Yeh, Solution strengthening of ductile refractory HfMo, NbTaTiZr high-entropy alloys, *Mater. Lett.* 175 (2016) 284–287, <http://dx.doi.org/10.1016/j.matlet.2016.03.133>.
- [52] E. Fazakas, V. Zadorozhnyy, L. Varga, A. Inoue, D. Louzguine-Luzgin, F. Tian, L. Vitos, Experimental and theoretical study of Ti₂₀Zr₂₀Hf₂₀Nb₂₀X₂₀ (X=V or Cr) refractory high-entropy alloys, *Int. J. Refract. Met. Hard Mater.* 47 (2014) 131–138, <http://dx.doi.org/10.1016/j.ijrmhm.2014.07.009>.
- [53] P.P.O. Borges, R.O. Ritchie, M. Asta, Local lattice distortions and the structural instabilities in bcc Nb-Ta-Ti-Hf high-entropy alloys: An ab initio computational study, *Acta Mater.* 262 (2024) 119415, <http://dx.doi.org/10.1016/j.actamat.2023.119415>.
- [54] T. Tsuru, S. Han, S. Matsuura, Z. Chen, K. Kishida, I. Iobzenko, S.I. Rao, C. Woodward, E.P. George, H. Inui, Intrinsic factors responsible for brittle versus ductile nature of refractory high-entropy alloys, *Nature Commun.* 15 (2024) 1706, <http://dx.doi.org/10.1038/s41467-024-45639-8>.
- [55] G. Dirras, L. Liliensten, P. Djemia, M. Laurent-Brocq, D. Tingaud, J.-P. Couzinié, L. Perrière, T. Chauveau, I. Guillot, Elastic and plastic properties of as-cast equimolar TiHfZrTaNb high-entropy alloy, *Mater. Sci. Eng. A* 654 (2016) 30–38, <http://dx.doi.org/10.1016/j.msea.2015.12.017>.
- [56] G. Laplanche, P. Gadaud, L. Perrière, I. Guillot, J.-P. Couzinié, Temperature dependence of elastic moduli in a refractory HfNbTaTiZr high-entropy alloy, *J. Alloys Compd.* 799 (2019) 538–545, <http://dx.doi.org/10.1016/j.jallcom.2019.05.322>.

- [57] R. Hill, The elastic behaviour of a crystalline aggregate, *Proc. R. Soc. Lond. Ser. A* 65 (1952) 349–354, <http://dx.doi.org/10.1088/0370-1298/65/5/307>.
- [58] E. Clouet, L. Ventelon, F. Willaime, Dislocation core energies and core fields from first principles, *Phys. Rev. Lett.* 102 (2009) 055502, <http://dx.doi.org/10.1103/PhysRevLett.102.055502>.
- [59] L. Dezerald, L. Ventelon, E. Clouet, C. Denoual, D. Rodney, F. Willaime, Erratum: Ab initio modeling of the two-dimensional energy landscape of screw dislocations in bcc transition metals [*Phys. Rev. B* 89 (2014) 024104], *Phys. Rev. B* 91 (2015) 019902(E), <http://dx.doi.org/10.1103/PhysRevB.91.019902>.
- [60] Z.-Q. Wang, Y.-H. Li, G.-H. Lu, H.-B. Zhou, Influence of carbon and oxygen on the core structure and Peierls stress of screw dislocation in molybdenum, *Metals* 12 (2022) 507, <http://dx.doi.org/10.3390/met12030507>.
- [61] M. Jiao, Z. Lei, Y. Wu, J. Du, X.-Y. Zhou, W. Li, X. Yuan, X. Liu, X. Zhu, S. Wang, H. Zhu, P. Cao, X. Liu, X. Zhang, H. Wang, S. Jiang, Z. Lu, Manipulating the ordered oxygen complexes to achieve high strength and ductility in medium-entropy alloys, *Nature Commun.* 14 (2023) 806, <http://dx.doi.org/10.1038/s41467-023-36319-0>.
- [62] A. Chen, Y. Pan, J. Dai, W. Fu, X. Song, Theoretical study on the element distribution characteristics and the effects of oxygen in TiZrHfNb high entropy alloys, *Mater. Today Commun.* 36 (2023) 106922, <http://dx.doi.org/10.1016/j.mtcomm.2023.106922>.